

# A discrete dislocation analysis of size-dependent plasticity in torsion

A. Cruzado<sup>1</sup>, M. P. Ariza<sup>2</sup>, A. Needleman<sup>3</sup>, M. Ortiz<sup>4</sup>, A. A. Benzerga<sup>1,3</sup>

<sup>1</sup>Department of Aerospace Engineering, Texas A&M University, College Station, TX 77843

<sup>2</sup>Escuela Técnica Superior de Ingeniería, Universidad de Sevilla, Sevilla 41092, Spain

<sup>3</sup>Department of Materials Science & Engineering, Texas A&M University, College Station, TX 77843

<sup>4</sup>Division of Engineering and Applied Science, California Institute of Technology, Pasadena, CA 91125

June 6, 2024

## Abstract

A method for solving three dimensional discrete dislocation plasticity boundary-value problems using a monopole representation of the dislocations is presented. At each time step, the displacement, strain and stress fields in a finite body are obtained by superposition of infinite body dislocation fields and an image field that enforces the boundary conditions. The three dimensional infinite body fields are obtained by representing dislocations as being comprised of points, termed monopoles, that carry dislocation line and Burgers vector information. The image fields are obtained from a three dimensional linear elastic finite element calculation. The implementation of the coupling of the monopole representation with the finite element method, including the interaction of curved dislocations with free surfaces, is presented in some detail because it differs significantly from an implementation with a line based dislocation representation. Numerical convergence and the modeling of dislocation loop nucleation for large scale computations are investigated. The monopole discrete dislocation plasticity framework is used to investigate the effect of size and initial dislocation density on the torsion of wires with diameters varying over three orders of magnitude. Depending on the initial dislocation source density and the wire diameter, three regimes of torsion-twist response are obtained: (i) for wires with a sufficiently small diameter, plastic deformation is nucleation controlled and is strongly size dependent; (ii) for wires with larger diameters dislocation plasticity is dislocation interaction controlled, with the emergence of geometrically necessary dislocations and dislocation pile-ups playing a key role, and is strongly size dependent; and (iii) for wires with sufficiently large diameters plastic deformation becomes less heterogeneous and the dependence on size is greatly diminished.

**Keywords:** Discrete Dislocation Plasticity, Size Dependence, Finite Element Analysis

# 1 Introduction

Plastic deformation arising from the evolution of dislocations is size dependent in micron scale metal crystals, see e.g. [Hutchinson \(2000\)](#). There are a variety of mechanisms that can lead to such size dependence with smaller being stronger. Some, for example, dislocation starvation and single arm dislocation source controlled plasticity at surfaces, can lead to size dependence when the imposed boundary conditions are consistent with homogeneous deformation ([Uchic et al., 2009](#), [El-Awady, 2015](#)). When the imposed boundary conditions and/or boundary constraints induce a deformation gradient, dislocation structures evolve that have a local net Burgers vector, the so-called Geometrically Necessary Dislocations (GNDs) ([Ashby, 1970](#)), give rise to long range stresses and induce a strong size effect. Examples of loadings and boundary constraints that lead to a strong size effect include indentation ([Nix and Gao, 1998](#), [Kysar et al., 2007](#)), beam bending ([Stölken and Evans, 1998](#), [Cleveringa et al., 1999](#)), torsion ([Fleck et al., 1994](#)), passivated thin films ([Nicola et al., 2006](#)), and in the vicinity of a crack tip or sharp notch ([Cleveringa et al., 2000](#)).

Dislocations in crystals are line defects. Hence, in mesoscale modeling of the evolution of dislocations in crystals, the dislocations are modeled as line defects in an elastic solid. In three dimensions, tracking the evolution of such lines is computationally complex ([Bulatov et al., 1998](#), [Zbib et al., 1998](#), [Ghoniem et al., 2000](#), [Arsenlis et al., 2007](#)). More recently, [Deffo et al. \(2019\)](#) have introduced an alternative description where the dislocation lines are carried by points, termed monopoles, and it is these points that must be kept track of, rather than the lines they carry. This has the potential for significantly simplifying mesoscale dislocation plasticity modeling.

In this study, torsion of single crystal wires is modeled using the monopole dislocation representation of [Deffo et al. \(2019\)](#), [Ariza and Ortiz \(2021\)](#). The method of monopoles may be regarded as a particle method applied to line dislocations, in which the dislocation line is concentrated at points, while simultaneously retaining local geometric information about the lines, namely length and direction, as well as local Burgers vector information. The collection of dislocation monopoles then supplies an approximation, in the sense of local averages, to the dislocation density, in the spirit of particle methods for mass transport ([Fedeli et al., 2017](#), [Carrillo et al., 2017, 2019](#), [Pandolfi et al., 2023](#)). The dislocation monopoles are updated in time according to linear-elastic energetic driving forces, a mobility law and geometric transformations that take into account the stretching of the dislocation lines due to curvature. These geometric updates encode the requirement that the monopoles approximate lines and, in particular, they ensure that the zero-divergence property of the dislocation density is satisfied approximately at all times. The method of monopoles effectively eschews the problems of line entanglement that inevitably arise in line-based representations and, as is commonly the case with particle methods, is remarkable for its ability to navigate through complex three-dimensional dislocation dynamics simply and without *ad hoc* rules.

Three dimensional quasi-static calculations are carried out, within the context of a small deformation formulation (geometry changes neglected), for wires with diameters ranging from 150nm to 10000nm. Various initial dislocation source densities are considered. Boundary conditions are imposed using the superposition method introduced by [Van der Giessen and Needleman \(1995\)](#) and, for line representation of dislocations, extended to three dimensions

by [Weygand et al. \(2002\)](#), [Crone et al. \(2014\)](#), [Joa et al. \(2023\)](#); also see ([Vattré et al., 2014](#), [Bertin et al., 2015](#)) for alternative methods. The monopole representation of dislocations requires a different treatment of dislocation-free boundary interactions than that given by [Weygand et al. \(2002\)](#) or more recent line-based methods.

Experimentally, a strong size effect in torsion of polycrystalline metal wires was documented by [Fleck et al. \(1994\)](#). Because wire torsion is an inherently three dimensional configuration, discrete dislocation modeling of wire torsion has only been carried out relatively recently by [Senger et al. \(2011\)](#), [Gravell and Ryu \(2020\)](#), and [Ryu et al. \(2020\)](#). These analyses were carried out for single crystals and used a line representation of the dislocations. As in the experiments of [Fleck et al. \(1994\)](#), a strong size effect was obtained.

The calculations here are carried out for wires with a circular cross section comprised of a single fcc crystal with properties representative of copper. Because implementation of the coupling between the monopole dislocation representation and the finite element method differs significantly from that for the line representation finite element coupling, the implementation of the coupling is described in some detail. Other aspects of the numerical implementation are discussed including consideration of numerical accuracy. Results are then presented for the effect of size on the moment-twist relation and for the effect of size on the dislocation structures that emerge. The variation of the scaling of the moment-twist relation with initial dislocation density is also illustrated.

## 2 Discrete dislocation plasticity framework

The three dimensional discrete dislocation plasticity formulation is based on the monopole representation of dislocations introduced by [Deffo et al. \(2019\)](#), also see [Ariza and Ortiz \(2021\)](#), together with the superposition of an image field following [Van der Giessen and Needleman \(1995\)](#) and [Weygand et al. \(2002\)](#). The presentation of the framework here focuses on the aspects particular to combining the monopole dislocation representation with the image field obtained from a finite element calculation.

A finite body occupying domain  $\Omega$  is subjected to boundary tractions  $\mathbf{T}_0$  on  $\partial\Omega_t$  and boundary displacements  $\mathbf{U}_0$  on  $\partial\Omega_u$ , as sketched in [Fig. 1](#). In its current state, the body contains a distribution of dislocation lines, collectively denoted  $C$ , carrying a Burgers vector  $\mathbf{b}(\mathbf{x})$  at every point  $\mathbf{x}$  of  $C$ . The dislocation network must be closed, i. e., the corresponding Nye’s dislocation density ([Nye, 1953](#)) must be divergence free, or terminate at the boundary of the solid. In addition, the Burgers vector  $\mathbf{b}(\mathbf{x})$  must be conserved along dislocation lines and satisfy Frank’s rule at branching points.

The procedure used to calculate the evolution in time of the dislocation configuration for given time-dependent boundary tractions and boundary displacements is described in the following sections.

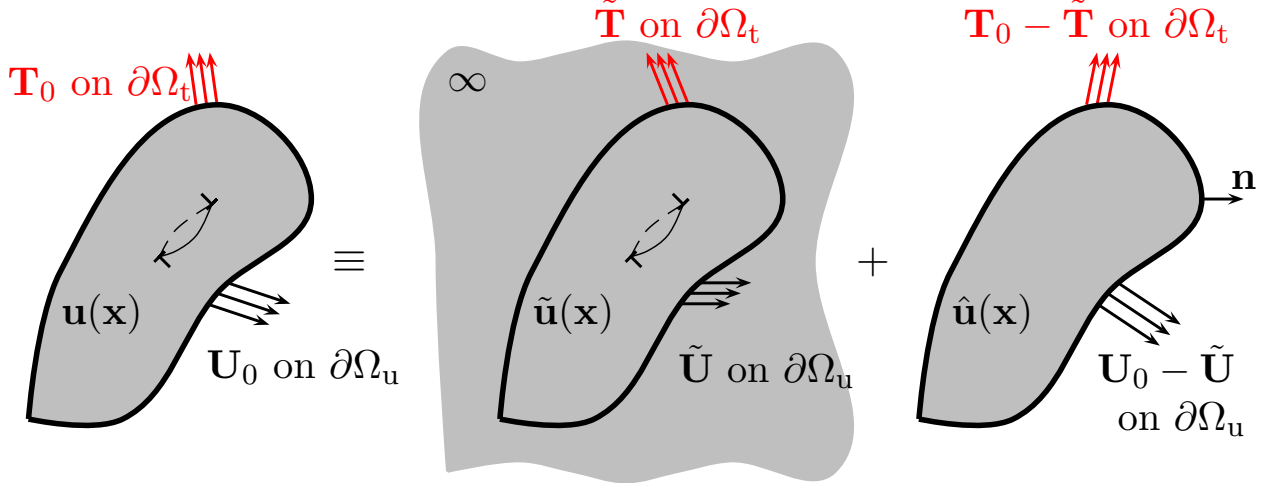


Figure 1: Decomposition of the problem into the superposition of interacting dislocations in a homogeneous infinite solid, the ( $\tilde{\cdot}$ ) fields, and the image problem that enforces the boundary conditions, the ( $\hat{\cdot}$ ) fields.

## 2.1 The monopole approximation

In calculations, we approximate the dislocation distribution by an ensemble of  $M$  monopoles labeled  $a = 1, \dots, M$ , with coordinates  $\{\mathbf{x}_a\}_{a=1}^M$ . The monopoles additionally carry corresponding elements of dislocation line  $\{\boldsymbol{\xi}_a\}_{a=1}^M$  and Burgers vector  $\{\mathbf{b}_a\}_{a=1}^M$ . The monopole ensemble approximates the dislocation line density in the sense that, for every continuous function  $\varphi_{ij}(\mathbf{x})$ ,

$$\oint_C \varphi_{ij}(\mathbf{x}) b_i(\mathbf{x}) dx_j \sim \sum_{a=1}^M \varphi_{ij}(\mathbf{x}_a) b_{ai} \xi_{aj}, \quad (1)$$

where we write  $b_{ai} := (\mathbf{b}_a)_i$  and  $\xi_{ai} := (\boldsymbol{\xi}_a)_i$ , and the error of the approximation can be controlled and made arbitrarily small by introducing a sufficiently large number of monopoles.

By Stokes' theorem, the divergence, or closedness condition of the dislocation line density, requires that

$$\oint_C \frac{\partial f_i}{\partial x_j}(\mathbf{x}) b_i(\mathbf{x}) dx_j = 0, \quad (2)$$

for every differentiable function  $f_i(\mathbf{x})$  with finite support. By the assumed approximation property, Eq. (1), it follows that, for a distribution of monopoles to represent an admissible distribution of closed dislocation lines, it must satisfy

$$\sum_{a=1}^M \frac{\partial f_i}{\partial x_j}(\mathbf{x}_a) b_{ai} \xi_{aj} \sim 0 \quad (3)$$

for every differentiable function  $f_i(\mathbf{x})$  with finite support, to within the level of approximation of the monopoles. This condition places a geometrical constraint on the distribution of monopoles that must be enforced at all times during the calculation by means of suitable geometric updates, cf. Section 2.3.

## 2.2 The instantaneous boundary-value problem

Suppose that the body is in equilibrium and the position of every monopole in the body is known. Superposition may then be used to write the displacement,  $\mathbf{u}$ , strain,  $\boldsymbol{\varepsilon}$ , and stress,  $\boldsymbol{\sigma}$ , fields as

$$\mathbf{u}(\mathbf{x}) = \tilde{\mathbf{u}}(\mathbf{x}) + \hat{\mathbf{u}}(\mathbf{x}); \quad \boldsymbol{\varepsilon} = \tilde{\boldsymbol{\varepsilon}} + \hat{\boldsymbol{\varepsilon}}; \quad \boldsymbol{\sigma} = \tilde{\boldsymbol{\sigma}} + \hat{\boldsymbol{\sigma}}, \quad (4)$$

where the symbol  $(\tilde{\cdot})$  refers to infinite-body fields and  $(\hat{\cdot})$  to image fields that enforce the boundary conditions, Fig. 1. By linearity, the infinite-body displacement and stress fields follow as

$$\tilde{\mathbf{u}}(\mathbf{x}) = \sum_{a=1}^M \mathbf{u}_a(\mathbf{x}), \quad \tilde{\boldsymbol{\sigma}}(\mathbf{x}) = \sum_{a=1}^M \boldsymbol{\sigma}_a(\mathbf{x}), \quad (5)$$

where  $\mathbf{u}_a(\mathbf{x})$  and  $\boldsymbol{\sigma}_a(\mathbf{x})$  are the contributions to the fields from monopole  $a$ , respectively. The corresponding expressions follow by inserting the approximation property Eq. (1) into well-known integral expressions from linear-elastic dislocation theory, cf., e. g., (Hirth and Lothe, 1982, Chapter 4), and are collected in the appendix, Eqs. (A-8) and (A-9), for completeness.

The  $(\hat{\cdot})$  fields are obtained from the solution of the linear elastic boundary value problem specified by

$$\nabla \cdot \hat{\boldsymbol{\sigma}} = \mathbf{0} \quad ; \quad \hat{\boldsymbol{\varepsilon}} = \nabla \otimes \hat{\mathbf{u}} \quad ; \quad \hat{\boldsymbol{\sigma}} = \boldsymbol{\mathcal{L}} : \hat{\boldsymbol{\varepsilon}} \quad \text{for } \mathbf{x} \in \Omega, \quad (6)$$

$$\mathbf{n} \cdot \hat{\boldsymbol{\sigma}} = \mathbf{T}_0 - \mathbf{n} \cdot \tilde{\boldsymbol{\sigma}} \quad \text{for } \mathbf{x} \in \partial\Omega_t \quad ; \quad \hat{\mathbf{u}} = \mathbf{U}_0 - \tilde{\mathbf{U}} \quad \text{for } \mathbf{x} \in \partial\Omega_u \quad (7)$$

with  $\boldsymbol{\mathcal{L}}$  the isotropic tensor of elastic moduli and  $\mathbf{n}$  the outer normal to  $\partial\Omega$ . Also,  $\tilde{\mathbf{U}}$  and  $\tilde{\mathbf{T}} = \mathbf{n} \cdot \tilde{\boldsymbol{\sigma}}$  are respectively the boundary displacement and traction arising from the infinite body dislocation fields (see Fig. 1),  $\nabla$  is the nabla operator and  $\otimes$  stands for the symmetric dyad. This boundary value problem is solved by the finite element method and traction boundary conditions are imposed through effective nodal forces. With  $\mathbf{F}_{0,\mathbf{n}}$  denoting the imposed nodal forces on a set  $\Gamma_f$  of boundary nodes lying on  $\partial\Omega_t$ , and with  $\hat{\mathbf{f}}_{\mathbf{n}}$  and  $\tilde{\mathbf{f}}_{\mathbf{n}}$  the corresponding nodal forces associated with the  $(\hat{\cdot})$  and  $(\tilde{\cdot})$  fields, the nodal forces imposed to obtain the image fields are

$$\hat{\mathbf{f}}_{\mathbf{n}} = \mathbf{F}_{0,\mathbf{n}} - \tilde{\mathbf{f}}_{\mathbf{n}}, \quad \mathbf{n} \in \Gamma_f \quad (8)$$

The values of the tilde forces  $\tilde{\mathbf{f}}_{\mathbf{n}}$  are obtained by assembling element nodal forces from all elements that have a boundary surface node. For each such element its contribution to the surface boundary nodal force is obtained by numerical integration of  $\tilde{\boldsymbol{\sigma}}(\mathbf{x})$  within that element.

## 2.3 Geometric updates

Suppose that the velocities  $\{\mathbf{v}_a\}_{a=1}^M$  of the monopoles are known. Then, the positions  $\{\mathbf{x}_a\}_{a=1}^M$  of the monopoles can be updated simply by time integration. However, in order to fully update the monopole configuration we additionally need update rules for the Burgers vectors  $\{\mathbf{b}_a\}_{a=1}^M$  and line elements  $\{\boldsymbol{\xi}_a\}_{a=1}^M$ . The update rules follow by time integration of the transport, or continuity, equation for the dislocation lines (cf. Mura (1982), Eqs. (32.2) and

(38.4)). For a distribution of monopoles, by the approximation property, Eq. (1), the discrete form of the transport equations becomes (Deffo et al., 2019, Ariza and Ortiz, 2021)

$$\dot{\mathbf{b}}_a = \mathbf{0}, \quad \dot{\boldsymbol{\xi}}_a = (\nabla \mathbf{v}_a) \boldsymbol{\xi}_a, \quad (9)$$

where  $\nabla \mathbf{v}_a$  is the gradient at  $\mathbf{x}_a$  of some suitable spatial interpolation of the monopole velocities  $\{\mathbf{v}_a\}_{a=1}^M$  and  $(\nabla \mathbf{v}_a) \boldsymbol{\xi}_a$  is the gradient of the velocity field in the direction of the line element  $\boldsymbol{\xi}_a$ .

It can be readily verified using the approximation property in Eq. (1) that the update of Eq. (9) properly accounts for the stretching and rotation of the line elements attendant to the motion of the monopoles (Ariza and Ortiz, 2021). In addition, it can also be verified (Deffo et al., 2019) that the update in Eq. (9) preserves dislocation loops remaining closed in the sense of Eq. (3). Thus, if the monopole ensemble initially approximates a closed distribution of dislocation lines, it still does so after the update, to within the accuracy of the monopole approximation and the velocity interpolation.

The computation of the velocity gradient requires an interpolation scheme of the general form

$$(\nabla \mathbf{v}_a)_{ij} = \sum_{b=1}^M v_{bi} \frac{\partial N_b}{\partial x_j}(\mathbf{x}_a). \quad (10)$$

where  $\{N_a(\mathbf{x})\}_{a=1}^M$  are suitable shape functions. In calculations we specifically use the max-ent shape functions (Arroyo and Ortiz, 2006)

$$N_a(\mathbf{x}) = \frac{1}{Z(\mathbf{x})} \exp\left(-\frac{\beta_a}{2} |\mathbf{x} - \mathbf{x}_a|^2\right), \quad Z(\mathbf{x}) = \sum_{a=1}^M \exp\left(-\frac{\beta_a}{2} |\mathbf{x} - \mathbf{x}_a|^2\right). \quad (11)$$

We note that the resulting interpolation, Eq. (10), is mesh-free and does not entail any ordering or connectivity between the monopoles. In Eq. (11), the distance  $1/\sqrt{\beta_a}$  sets the range of interaction for monopole  $a$ . Thus, only those monopoles that are at a distance of order  $1/\sqrt{\beta_a}$  ‘see’ and interact with monopole  $a$ . In practice, this property can be exploited to reduce the range of the sums in Eq. (10) and Eq. (11).

The effect of the shape functions  $N_a(\mathbf{x})$  is to broaden the monopoles and give them a spatial profile of finite width  $1/\sqrt{\beta_a}$ . This broadening allows neighboring monopoles to ‘see’ each other for purposes of the interpolation of their velocities into a continuous velocity field, which in turns governs the geometrical update of the line elements  $\{\boldsymbol{\xi}_a\}_{a=1}^M$  per Eq. (9). In this sense, the broadening of the monopoles is analogous to finite-particle, or ‘blob’, methods for problems of mass transport (Carrillo et al., 2019, Pandolfi et al., 2023).

## 2.4 Mobility

In order to close the evolution problem, a mobility law for the velocity of the monopoles is required. The motion of the monopoles is taken to be driven by the configurational Peach-Koehler force to account for a change in position of the dislocation as well as the self force associated with the energy cost of a change in dislocation line length, so that

$$\mathbf{f}_a = (\boldsymbol{\sigma}(\mathbf{x}_a) \cdot \mathbf{b}_a) \times \boldsymbol{\xi}_a, \quad (12)$$

or, in view of Eq. (4) and Eq. (5),

$$\mathbf{f}_a = (\hat{\boldsymbol{\sigma}}(\mathbf{x}_a) \cdot \mathbf{b}_a) \times \boldsymbol{\xi}_a + \sum_{b=1}^M (\boldsymbol{\sigma}_b(\mathbf{x}_a) \cdot \mathbf{b}_a) \times \boldsymbol{\xi}_a. \quad (13)$$

The driving force  $\mathbf{f}_a$  comprises one term contributed by the image stresses, which in turn accounts for boundary effects and the finiteness of the domain, and a second term resulting from the elastic interaction between the monopoles.

However, a direct evaluation of the self-force terms,  $b = a$  in Eq. (13), from linear elasticity is not possible since  $\boldsymbol{\sigma}_a(\mathbf{x})$  diverges as  $\mathbf{x}$  approaches  $\mathbf{x}_a$ . The singularity can be removed by fitting the monopoles with a core profile of a width  $\epsilon$  commensurate with a lattice parameter (Bulatov and Cai, 2006, Lazar, 2017, Deffo et al., 2019). A particular core profile, and the attendant regularization of monopole self-forces, can be achieved by recourse to strain-gradient elasticity (Deffo et al., 2019). The resulting expressions are collected in Appendix A for completeness.

Once a suitably regularized set of monopole forces has been defined, the velocity of the monopoles can be computed from a mobility law of the type

$$\mathbf{v}_a = \mathbf{M}_a \mathbf{f}_a, \quad (14)$$

where  $\mathbf{M}_a$  is a mobility tensor. In general, the edge and screw mobilities of glide dislocations, as well as the climb mobilities, differ greatly in actual crystals, and this renders the mobility tensor  $\mathbf{M}_a$  anisotropic. More general mobility laws, including nonlinearity, can be treated likewise (Deffo et al., 2019, Ariza and Ortiz, 2021).

## 2.5 Calculation of image forces

Determining the first term in Eq. (12),  $\hat{\mathbf{f}}_a$ , requires evaluating the image stress, determined by solving Eqs. (6) and (7), at the location of monopole  $a$ . This is accomplished by interpolating the  $\hat{\boldsymbol{\sigma}}$  field to the position of the monopole. During the deformation history, monopoles change elements. An efficient ( $\mathcal{O}(\log M)$  operations) binary B-tree algorithm (Comer, 1979) (so-called BB-tree (Z-set, 2020)) is used as an element locator to obtain the monopole coordinates  $\mathbf{x}_a$  within an element. Because the  $\hat{\boldsymbol{\sigma}}$  field is discontinuous across element boundaries, the values of  $\hat{\boldsymbol{\sigma}}$  are extrapolated to element nodes using the finite element shape functions. Then the nodal values of  $\hat{\mathbf{f}}_a$  are averaged over all elements sharing the same node, before interpolation to the monopoles.

## 2.6 Topological transitions

Because the infinite body dislocation expressions pertain to a closed line, a key issue in the numerical implementation of discrete dislocation dynamics in finite bodies is the treatment of cases where part of a dislocation loop exits the body, as illustrated in Fig. 2a. To address this within the context of the monopole representation of dislocations, a method involving virtual monopoles is introduced, akin to virtual segments employed in line-based methods

(Weygand et al., 2002, Liu et al., 2005, Weinberger et al., 2009, Deng et al., 2008, Leiter et al., 2013, Crone et al., 2014).

At each time step in the calculation, monopoles associated with a dislocation loop that have exited the body, as shown in Fig. 2a, are identified. Then the two monopoles of that loop that remain in the body and that are closest to the surface are detected, see Fig. 2b. The distance between these two dislocations is denoted by  $d_{1-2}$ . Virtual monopoles are introduced to close the loop as illustrated in Fig. 2c. The monopoles shown black in Fig. 2a are removed from subsequent calculations of the dislocation dynamics. The virtual monopoles shown in red in Fig. 2c are only used to calculate the tilde fields in Eqs. (5) and (12). In the computations here 10 virtual monopoles lying on a semi-circle of radius equal to half the distance  $d_{1-2}$  are added.

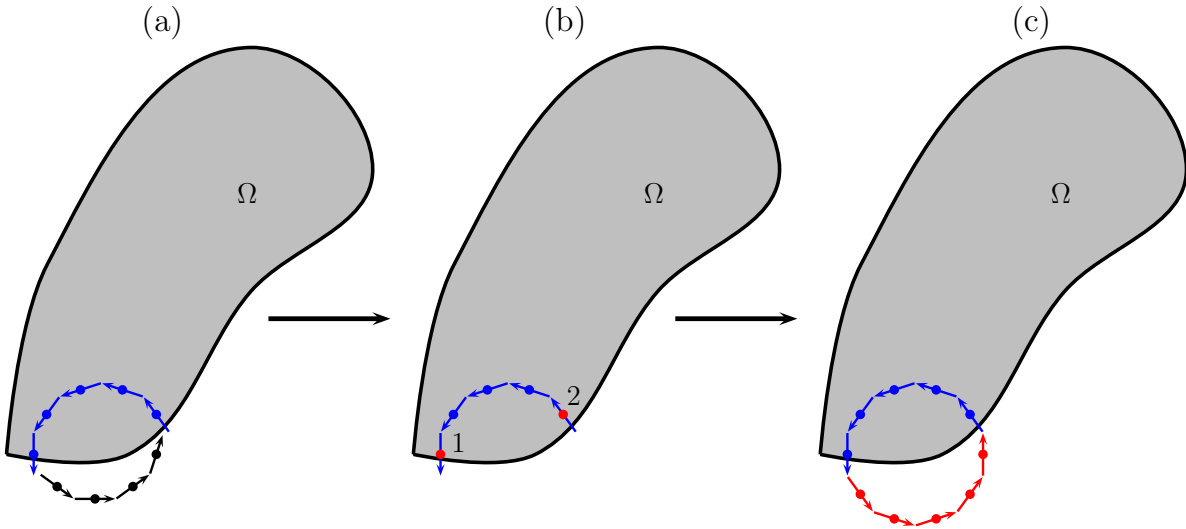


Figure 2: Schematic of a dislocation loop exiting the free surface and the introduction of virtual monopoles in three steps: (a) Step 1: check for monopoles that are outside the body  $\Omega$  (black) and remove them. (b) Step 2: identify the two monopoles that are closest to the surface. (c) Step 3: create virtual monopoles (red) and the corresponding element of line  $\xi$  that closes the loop.

Dislocation nucleation/multiplication is included in the calculations via a source model (Deffo et al., 2019). The locations of potential sources are randomly distributed in the body prior to the start of the calculation of the deformation history. Each potential source is defined as a set of monopoles arranged in a loop. At a given source location, a loop of radius  $r_0$  nucleates when

$$\alpha|\hat{\mathbf{f}}_a| - |\mathbf{f}_a^\epsilon| > 0, \quad \forall a \in M(r_0), \quad (15)$$

with  $M(r_0)$  denoting the set of monopoles defining the loop and  $\alpha > 0$  a parameter. Here,  $\mathbf{f}_a^\epsilon$  denotes the second term in Eq. (12), regularized using a core parameter  $\epsilon$ ; see Appendix A. Eq. (15) states that the external force acting on each monopole must exceed its internal force so that the loop does not collapse. Once this condition is met, the source emits a dislocation loop so that the new monopoles that comprise the nucleated loop are inserted into the calculation.



## 2.7 Coupled time-integration algorithm

For given domain geometry and forcing, Eqs. (9), (13) and (14) govern the evolution of the monopole ensemble. Time integration may be accomplished using standard time-stepping algorithms, such as fully implicit backward-Euler (Deffo et al., 2019) or explicit two-stage Runge-Kutta method (Ariza and Ortiz, 2021).

The computational method involves the following steps:

1. At time  $t$  the body is in equilibrium and the position of each monopole in the body is known. The surface nodal forces  $\tilde{\mathbf{f}}$  corresponding to  $\tilde{\boldsymbol{\sigma}}$  and displacements  $\tilde{\mathbf{u}}$  are computed.
2. The boundary-value problem defined by Eqs. (6) and (7) for the  $(\hat{\cdot})$  fields is solved.
3. The  $\hat{\boldsymbol{\sigma}}$  field is interpolated to the monopole locations to evaluate the Peach-Koehler forces  $\{\mathbf{f}_a\}_{a=1}^M$  in Eq. (12). This interpolation is performed for both static source locations to evaluate the nucleation criterion, Eq. (15), and for existing monopoles.
4. The condition for new loop nucleation, Eq. (15), is checked.
5. The rate equations Eq. (9), Eq. (13) and Eq. (14) are integrated in time to determine new monopole configurations at time  $t + \Delta t$ .
6. Monopoles that lie outside the body are flagged and removed. Virtual monopoles are added to close the dislocation loop for stress calculations.
7. Go to step 1 with  $t \leftarrow t + \Delta t$ .

The code used to solve the initial/boundary value problem is a combination of the serial MonoDis code of Deffo et al. (2019), Ariza and Ortiz (2021) and the Z-set (Z-set, 2020) finite element code. These are integrated through a C++ plug-in interface. The implementation has the following features: (i) for the linear elastic finite element calculations, Cholesky decomposition of the global stiffness matrix is carried out once, (ii) expressions derived from the principle of virtual work are used to enforce the traction and displacement boundary conditions, and (iii) the image force interpolation uses a BB-tree algorithm. Because inversion of the global stiffness matrix is executed only once, the time used for the finite element part solution is a small part of the total computational time for calculation of the deformation history.

## 3 Torsion problem formulation

Calculations were carried out on cylindrical specimens characterized by diameters  $D$  ranging between  $0.15\mu\text{m}$  and  $10\mu\text{m}$  and a length to diameter ratio  $L/D = 3.5$ . Torsion boundary conditions were applied via an applied twist angle, with  $\mathbf{e}_z$  being a unit vector along the axis of twist, Fig. 3a. The top surface (at  $z = L/2$ ) was subjected to twist angle  $\theta$  while all nodes of the bottom surface (at  $z = -L/2$ ) were fixed, Fig. 3a. A linear approximation was

employed where  $\sin \theta \approx \theta$ , suitable for small strain problems. The specimens were loaded with a constant torsion rate of  $\dot{\varphi} \approx 5.6^\circ \text{ ns}^{-1}$ .

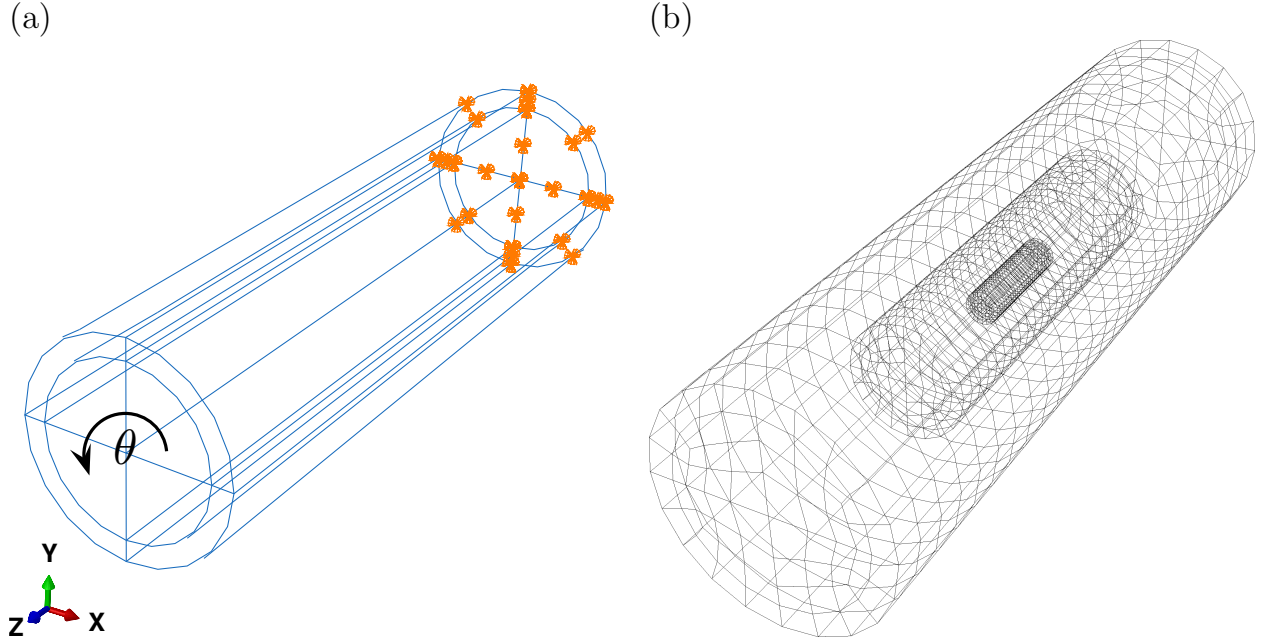


Figure 3: (a) Boundary-value problem for torsion of an fcc single crystal wire subjected to a prescribed twist angle  $\theta$ . In the calculations, the wire is taken to have a  $[001]$  orientation. (b) Example finite element meshes for wire diameters of  $D = 150\text{nm}$ ,  $500\text{nm}$ , and  $1000\text{nm}$ , nested into each other.

A relatively coarse mesh was used for all specimens, as illustrated in Fig. 3b. An analysis of mesh refinement and element type was carried out; see Section 3.1. On that basis, most calculations were performed using meshes consisting of 1664 20 node brick elements with quadratic displacement shape functions and 27 point Gaussian integration.

The centers of dislocation sources were randomly dispersed along the axial and hoop directions, but they were located radially at  $D/2 - e$  from the surface, where  $e$  denotes an exclusion distance, Fig. 4. In the calculations here,  $e = 2r_0$  with  $r_0$  being the initial loop radius. The number of sources was adjusted so as to achieve a desired initial dislocation density  $\rho_0$ . At nucleation, the radius of initial loops is scaled with the specimen size as  $r_0 = D/10$ . Each loop is discretized using line element lengths  $\xi = |\xi_a| = 2 \pi r_0 / M(r_0)$ . Also, no monopole splitting was used in any of the calculations.

A time step of  $\Delta t = 0.3 \text{ ps}$  was chosen based on numerical stability considerations (Ariza and Ortiz, 2021), derived from the smallest dislocation loop ( $r_0 = 15 \text{ nm}$  for a wire diameter of  $D = 150 \text{ nm}$ ).

The material parameters were chosen to be representative of copper but with isotropic elastic properties, shear modulus  $G = 48\text{GPa}$ , and Poisson's ratio  $\nu = 0.34$ . The Burgers vector length is taken to be  $b = 0.2556 \text{ nm}$ , and lattice parameter is  $a = 0.3614 \text{ nm}$ . Only dislocation glide is considered in the calculations and the relation between glide component  $f_{\text{glide}}$  of  $\mathbf{f}_a$  in Eq. (13) and dislocation glide velocity  $v_{\text{glide}}$  is taken to be independent of

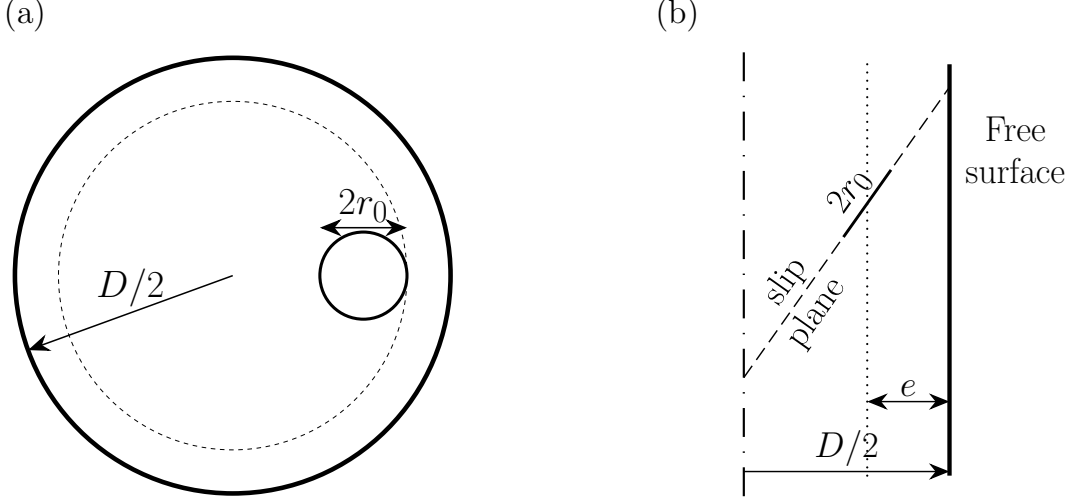


Figure 4: Illustration of the exclusion distance  $e$ . (a) Sketch of a dislocation loop in a transverse plane of the wire; (b) Sketch of a dislocation loop on a slip plane inclined relative to the wire axis.

dislocation character and given by

$$v_{\text{glide}} = \frac{1}{B} f_{\text{glide}} \quad (16)$$

with the glide mobility constant taken to be  $B = 10^{-5} \text{ Pa s}^{-1}$ .

Results are presented in terms of the normalized torque,  $T/D^3$ , versus plastic strain on the surface,  $\gamma_{\text{surf}}^p$ . The net torque at any given time  $t$  is calculated using:

$$\mathbf{T} = \sum_{n=1}^{N_{\text{surfz}+}} \mathbf{x}_n \times \hat{\mathbf{f}}_n + \left[ \sum_{n=1}^{N_{\text{surfz}+}} \mathbf{x}_n \times \tilde{\mathbf{f}}_n - \sum_{n=1}^{N_{\text{surfz}-}} \mathbf{x}_n \times \tilde{\mathbf{f}}_n \right] \quad (17)$$

where  $\mathbf{x}_n$  denotes the position of surface node  $n$  relative to the axis of torque,  $N_{\text{surfz}+}$  denotes the nodes corresponding to the positive  $z$  face, and  $N_{\text{surfz}-}$  corresponds to the negative  $z$  face. The first term in Eq. (17) represents the net torque computed from the finite element solution, which is opposite and equal in magnitude to the reaction torque at the bottom surface. The second, bracketed term in Eq. (17) represents a correction torque arising from the symmetry breaking due to random dislocation locations.

The incremental plastic twist per unit length,  $\Delta\theta^p$ , due to dislocation motion, is obtained from

$$\Delta\theta^p = \frac{\Delta\varphi}{L} = \sum_a^M \frac{1}{I_p L} - (b_z^a \nu_x^a + b_x^a \nu_z^a) \bar{y}^a + (b_z^a \nu_y^a + b_y^a \nu_z^a) \bar{x}^a \Delta A_{\text{swept}}^a \quad (18)$$

which is adapted from a similar equation used by [Ryu et al. \(2020\)](#). Here,  $\bar{x}^a$  and  $\bar{y}^a$  denote the centroid locations of the swept area of the  $a$ th monopole element of line,  $I_p = \pi R^4/2$  is the polar moment of inertia, and  $\nu_i$  are the components of the slip plane normal. The surface shear strain,  $\gamma_{\text{surf}}^p$ , is defined as

$$\gamma_{\text{surf}}^p = \Delta\theta^p \left( \frac{D}{2} \right) \quad (19)$$

### 3.1 Numerical aspects

First, the optimal size of the element of dislocation line  $\xi$ , needed to accurately reproduce the non-singular solution for (isolated) general dislocation loops (Cai et al., 2006, Hirth and Lothe, 1982) is explored. Fig. 5a shows the shear stress, defined based on the average Peach-Koehler force

$$\tau = \frac{1}{M} \sum_a^M |\mathbf{f}_a^e|/b \quad (20)$$

versus the loop radius for various values of  $\xi$  using a core regularization parameter  $\epsilon = 2b$ . A value of  $\xi = 0.86b$  is needed to recover the analytical solution of the general loop. For larger loops, this value of  $\xi$  leads to a large number of monopoles being required. In order to reduce the computational time, a scaling relation between  $\xi$  and  $\epsilon$  is used. This enables calculations with larger values of  $\xi$  to be used while maintaining accuracy as illustrated in Fig. 5b.

In the calculations here, the values of  $\xi$  and  $\epsilon$  are set for  $r_0 = 15$  nm and then proportionally scaled with the dislocation loop radius. This maintains accuracy for the value of the resolved shear stress of a general loop of radius  $r_0$  (Fig. 5b). As a result, only 10 monopoles are needed for both, a  $r_0 = 15$  nm dislocation loop nucleated at wire diameters of  $D = 150$  nm and a  $r_0 = 1000$  nm loop nucleated at  $D = 10000$  nm. This reduces the computational time needed for larger specimens by at least an order of magnitude.

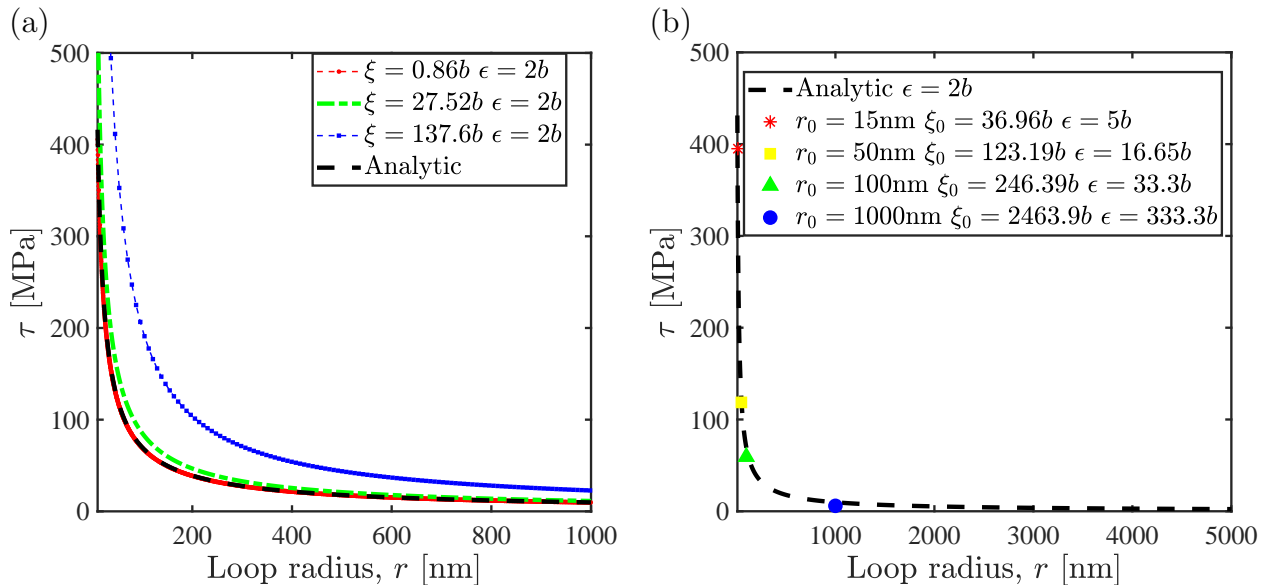


Figure 5: Plots of resolved shear stress,  $\tau$ , for a general dislocation loop, defined by Eq. (20) versus loop radius  $r$ . (a) Comparison of the monopole discretization results with the analytical solution of Hirth and Lothe (1982) for current line element values  $\xi = 0.86b$ ,  $\xi = 27.52b$  and  $\xi = 137.6b$ . The value of the regularization parameter  $\epsilon$  is fixed at  $2b$ . (b) The effect of the choice of initial values of line element  $\xi_0$  and choice of the value of the regularization parameter  $\epsilon$  for dislocation loops with various values of initial radius  $r_0$ .

Next, presume that loop nucleation occurs when the externally applied stress exceeds the equilibrium shear stress of a loop with radius  $r_0$ , as inferred from Fig. 5b. This would correspond to using  $\alpha = 1$  in Eq. (15). Calculations showed that this condition can lead to high curvature-driven shape instabilities, as illustrated in Fig. 6a, causing the loop to partially collapse and resulting in numerical convergence issues. Stable growth of dislocation loops was found to occur using  $\alpha \geq 1.5$ . Some examples are shown in Fig. 6b and Fig. 6c. In all subsequent calculations the value  $\alpha = 1.5$  has been used.

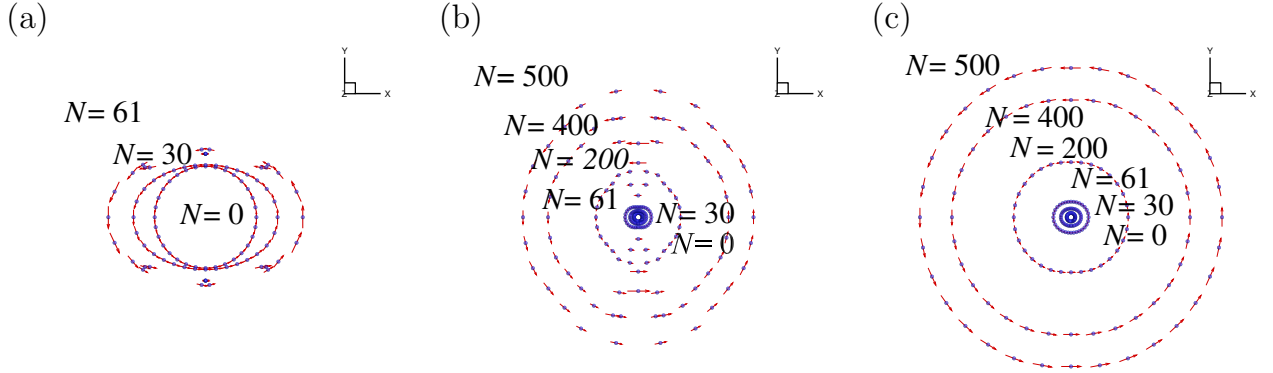


Figure 6: Monopole configurations at various time increments  $N$  for an initially circular loop of radius  $150b$  subject to a remote shear stress using (a)  $\alpha = 1$ , (b)  $\alpha = 1.25$ , and (c)  $\alpha = 1.5$  in Eq. (15).

The effect of free surfaces is now analyzed by comparing with a result of Weygand et al. (2002) for a circular loop with radius  $r = 4000a$ , and Burgers vector  $\mathbf{b} = a[100]/\sqrt{2}$ , placed at the center of a cube with side length  $l = 10000a$  that lies in the  $x - z$  plane. All surfaces of the cube are free of tractions. The loop was discretized using  $\xi = 1185b$  and  $\epsilon = 100b$ .

In these calculations, two types of spatial discretization were used: 20 node brick elements with quadratic displacement shape functions and 27 point Gaussian integration, as well as 8 node brick elements with linear displacement shape functions and 8 point Gaussian integration.

Fig. 7a shows the norm of the infinite body Peach–Koehler force,  $\tilde{\mathbf{f}}_a$ , and the norm of the finite element computed image force,  $\hat{\mathbf{f}}_a$ , per monopole as the length of the loop is spanned starting at the screw segment. Results are shown for the two types of finite elements and various mesh densities denoted by the cube of the number of elements per side of the cube. For reference, the 8 elements per side and 64 elements per side correspond to element sizes of  $883b$  and  $110b$ , respectively. Using quadratic elements (denoted by C3D20 in Fig. 7a), convergence is attained for 16 elements per side (an element size of  $441b \sim 100\text{nm}$ ), which is approximately half the size of the line elements used to discretize the loop. On the other hand, no convergence was obtained using the linear elements (denoted by C3D8 in Fig. 7a) up to 64 elements per side.

It was verified that the hat component of the resolved shear stress,  $\hat{\tau} = -n_i \hat{\sigma}_{ij} b_j / b$ , matches the numerical solution obtained by Weygand et al. (2002) using a line-based method, as shown in Fig. 7b.

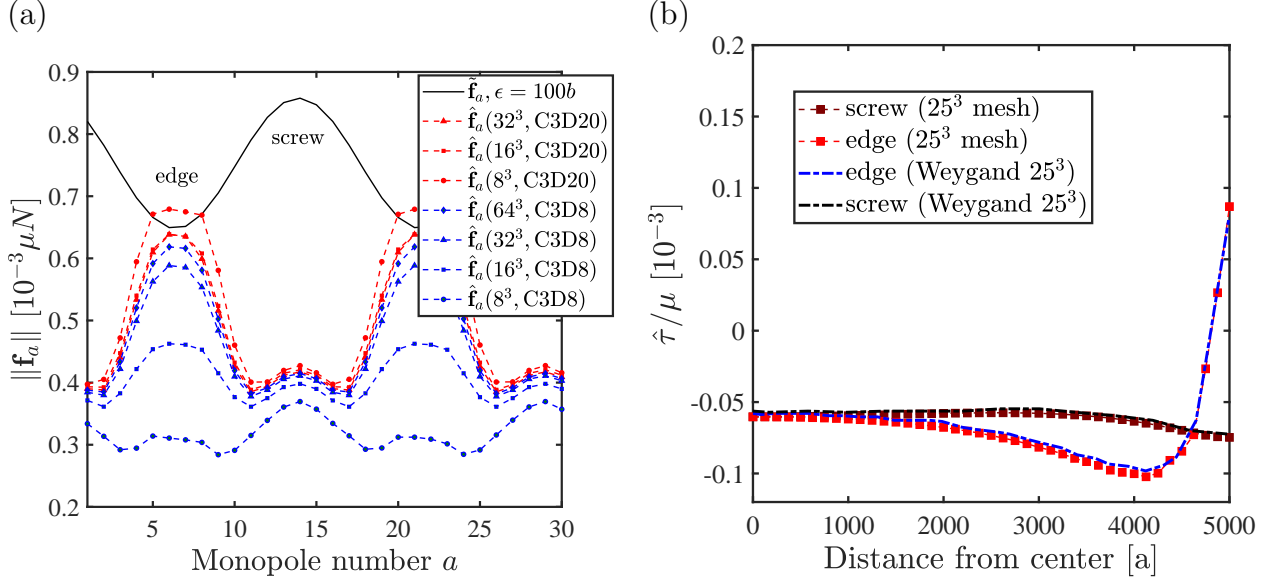


Figure 7: (a) Glide component of the Peach-Koehler force around a dislocation loop versus the number of monopoles used to represent the loop for various finite element mesh discretizations. The number in parenthesis is the number of elements per side of the cube and C3D20 and C3D8 denote 20 node and 8 node finite element shape functions, respectively. (b) The image shear stress,  $\hat{\tau}$ , in the glide plane along a path that extends from the center of the dislocation loop through the purely edge-oriented and screw-oriented parts of the dislocation to the free surface of the cube compared with the results of [Weygand et al. \(2002\)](#) with a finite element discretization of 25 elements per side.

## 4 Results

The normalized torque,  $T/D^3$ , where  $T = |\mathbf{T} \cdot \mathbf{e}_z|$  is the torque calculated using Eq. (17) and  $D$  is the wire diameter, is plotted in Fig. 8 versus the average surface plastic strain,  $\gamma_{\text{surf}}^p$ , given by Eq. (19). Calculations were carried out for 5 to 10 realizations with the same wire diameter and initial density of dislocation sources. In all calculations, the fcc single crystal wires are taken to have a [001] orientation. Two values of initial dislocation source density were considered: (i) an initial dislocation source density of  $\rho_0 = 6 \times 10^{13} \text{ m}^{-2}$  for wire diameters in the range  $D = 150\text{--}1000 \text{ nm}$ ; and (ii) a smaller value of initial dislocation source density,  $\rho_0 = 1 \times 10^{11} \text{ m}^{-2}$ , for wire diameters in the range  $D = 1000\text{--}10000 \text{ nm}$ .

Fig. 8a shows the normalized torque versus average plastic strain at the surface for wires with diameters in the range between  $D = 150 \text{ nm}$  and  $D = 1000 \text{ nm}$ . For each wire diameter the response is plotted for all realizations analyzed. The normalized torque at  $\gamma_{\text{surf}}^p = 0.2\%$  increases from about 60 MPa for  $D = 1000 \text{ nm}$  to 250 MPa for  $D = 150 \text{ nm}$  with the variation in response with realization being greater for smaller values of wire diameter. This variation with wire diameter is similar to that found by [Ryu et al. \(2020\)](#).

The evolution of the mean dislocation density  $\rho$  for wire diameters ranging from  $D = 150 \text{ nm}$  to  $D = 1000 \text{ nm}$  is shown in Fig. 8b. The formation of geometrically necessary dislocations (GNDs) leads to a higher mean dislocation density with increasing values of

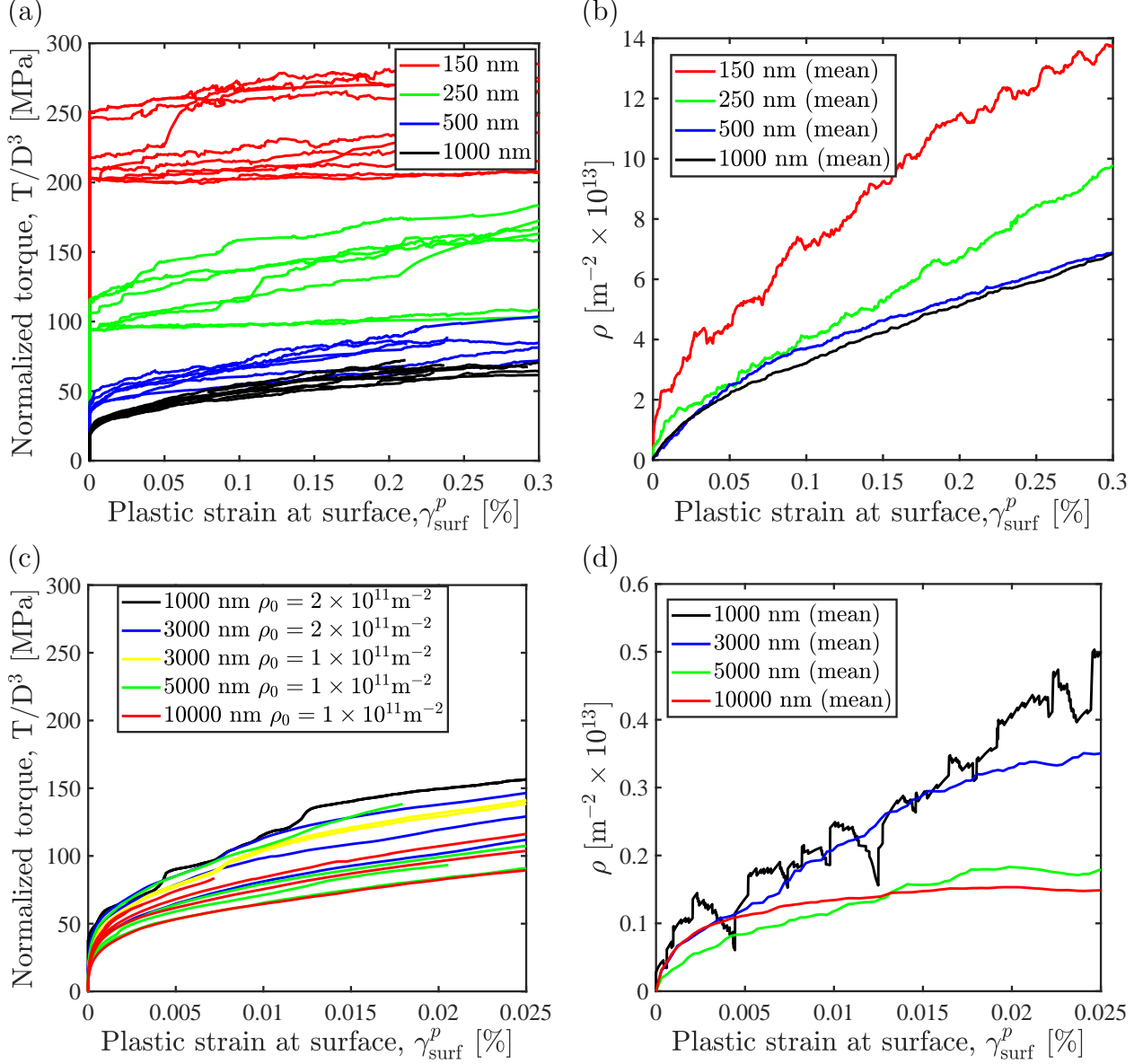


Figure 8: (a) Normalized torque,  $T/D^3$ , versus surface plastic strain,  $\gamma_{\text{surf}}^p$ , and (b) dislocation density versus  $\gamma_{\text{surf}}^p$ , for an initial dislocation density  $\rho_0 = 6 \times 10^{13} \text{m}^{-2}$  and for wire diameters  $D = 150, 250, 500, 1000$  nm. (c) Normalized torque,  $T/D^3$ , versus surface plastic strain,  $\gamma_{\text{surf}}^p$ , and (b) dislocation density versus  $\gamma_{\text{surf}}^p$ , for an initial dislocation density  $\rho_0 = 0.01 - 0.02 \times 10^{13} \text{m}^{-2}$  and for wire diameters  $D = 1000, 3000, 5000, 10000$  nm.

$\gamma_{\text{surf}}^p$  and therefore with torque  $T$ . The dislocation density increases more rapidly with  $\gamma_{\text{surf}}^p$  for  $D = 150$  nm than for the wires with larger diameters. In the calculations here, the linear proportional relation between dislocation density and the surface plastic strain, seen by Senger et al. (2011), Ryu et al. (2020) is not obtained.

Figs. 8c and 8d, respectively, show the normalized torque,  $T/D^3$ , versus average surface plastic strain  $\gamma_{\text{surf}}^p$  response and the evolution of dislocation density for wires with diameters

in the range  $D = 1000$  nm to  $D = 10000$  nm. For larger diameter wires the curves of  $T/D^3$  versus  $\gamma_{\text{surf}}^p$  show less variation with realization and are smoother, i.e. there are fewer strain bursts, than the corresponding curves for smaller diameter wires in Fig. 8a. For these larger diameter wires, there is still some size effect but it is much less pronounced than for the smaller diameter wires.

The scaling of the normalized torque with size, i.e. with the wire diameter  $D$ , is shown in Fig. 9 which is a log-log plot of the average value over all realizations calculated of  $T/D^3$  at a specified value of  $\gamma_{\text{surf}}^p$  versus the wire diameter  $D$ . One curve is for wires with diameters ranging from  $D = 150$  nm to  $D = 1000$  nm, with an initial dislocation source density of  $\rho_0 = 6 \times 10^{13} \text{ m}^{-2}$  and a torque evaluated at  $\gamma_{\text{surf}}^p = 0.2\%$ . The other curve is for wires with diameters ranging from  $D = 1000$  nm to  $D = 10000$  nm, with an initial dislocation source density of  $\rho_0 = 1 \times 10^{11} \text{ m}^{-2}$  and with the torque evaluated at  $\gamma_{\text{surf}}^p = 0.02\%$ .

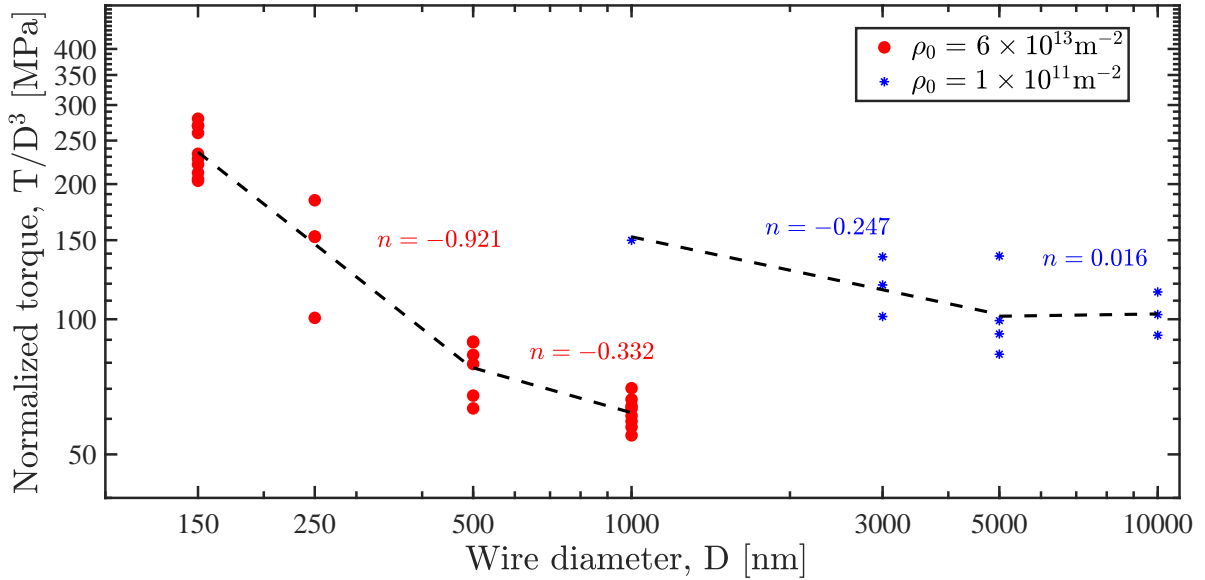


Figure 9: Log-log plots of normalized torque,  $T/D^3$ , versus wire diameter  $D$  for single crystal fcc wires subject to a prescribed twist. Results are shown for two values of initial dislocation density,  $\rho_0$ . For  $\rho_0 = 6 \times 10^{13} \text{ m}^{-2}$  the values of  $T/D^3$  are at a surface plastic strain of  $\gamma_{\text{surf}}^p = 0.2\%$  with wire diameters of  $D = 150, 250, 500, 1000$  nm. For  $\rho_0 = 1 \times 10^{11} \text{ m}^{-2}$  the values of  $T/D^3$  are at a surface plastic strain of  $\gamma_{\text{surf}}^p = 0.02\%$  with wire diameters of  $D = 1000, 3000, 5000, 10000$  nm.

For both the smaller wires and the larger wires, the size dependence can be characterized by a bilinear fit. For wire diameters in the range from  $D = 150$  nm to  $D = 1000$  nm, for those with  $150 \text{ nm} \leq D \leq 500 \text{ nm}$  the fit exponent is  $n = -0.912$  and for wire diameters in the range from  $D = 500$  nm to  $D = 1000$  nm the fit exponent is  $n = -0.332$ . While for the wires with the small values of initial dislocation source density, which have diameters ranging from  $1000$  nm to  $10000$  nm, the two exponents fit are  $n = -0.247$  and  $n = 0.016$ , indicating that for a sufficiently large wire diameter, the response is predicted to be nearly size independent. Thus, our results indicate that the exponent characterizing the size effect in torsion of single crystal wires is dislocation source density dependent as well as size dependent. The values of



the exponents characterizing the size dependence in previous discrete dislocation plasticity analyses of wire torsion were  $n = -0.96$  by [Senger et al. \(2011\)](#) and  $n = -0.417$  by [Ryu et al. \(2020\)](#). The largest wire diameter considered by [Senger et al. \(2011\)](#) was  $1\mu\text{m}$  and the largest wire diameter considered by [Ryu et al. \(2020\)](#) was  $2\mu\text{m}$ .

To gain insight into the bilinear size dependence, contours of the von Mises effective stress, defined by

$$\sigma_e = \sqrt{\boldsymbol{\sigma}' : \boldsymbol{\sigma}'} \quad , \quad \boldsymbol{\sigma}' = \boldsymbol{\sigma} - \frac{1}{3}\text{tr}(\boldsymbol{\sigma})\mathbf{I}, \quad (21)$$

are shown in Fig. 10 at  $\gamma_{\text{surf}}^p = 0.21\%$  for wires with three values of wire diameter,  $D = 150$  nm in Fig. 10a,  $D = 500$  nm in Fig. 10b and  $D = 1000$  nm in Fig. 10c. Recall that the meshes used are relatively coarse so that the stresses are actually more concentrated than shown in the figure. The main effect in Fig. 10 is that the high values of Mises effective

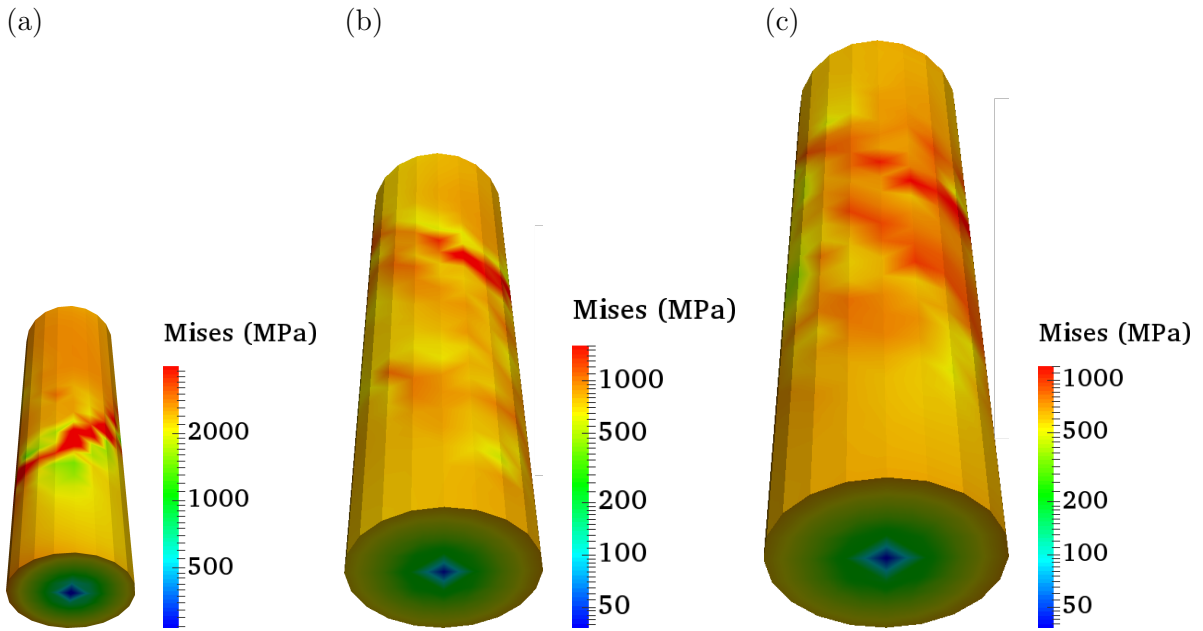


Figure 10: Contours of Mises effective stress, Eq. (21), illustrating increasing localization in a band with decreasing wire diameter  $D$  at  $\gamma_{\text{surf}}^p = 0.21\%$  for  $\rho_0 = 6 \times 10^{13} \text{ m}^{-2}$  and for various wire diameters. (a)  $D = 150$  nm, (b)  $D = 500$  nm and (c)  $D = 1000$  nm.

stress are in a single band for  $D = 150$  nm and that the distribution of Mises effective stress becomes more uniformly distributed for the larger values of  $D$ . The change in slope in Fig. 9 is associated with the change from a nucleation-controlled, localized distribution of plasticity to one that is more uniformly distributed. Also, for all three values of wire diameter, there is a radial gradient of the Mises effective stress, which varies from near zero in the center of the wire to its maximum value at the surface.

Fig. 11 shows the dislocation structure for the three cases in Fig. 10. With  $D = 150\text{nm}$  (Fig. 11a), only a few dislocation sources on a few glide planes are activated initially. With increasing twist, plastic deformation predominantly involves source nucleation, and then subsequently dislocation exhaustion occurs due to dislocations exiting the free surface ([Greer et al., 2005](#), [Benzerga, 2008](#)). This can lead to an abrupt increase in the value of normalized

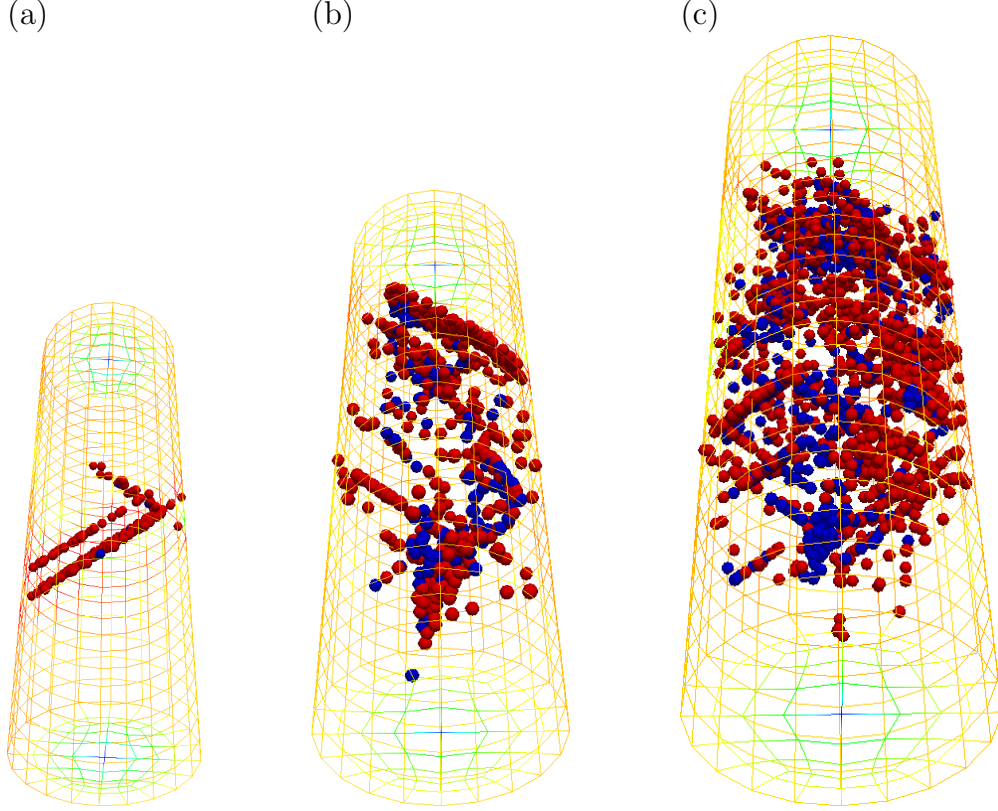


Figure 11: Monopole locations showing the dislocation network with  $\rho_0 = 6 \times 10^{13} \text{ m}^{-2}$  at  $\gamma_{\text{surf}}^p = 0.21\%$  and with wire diameters: (a)  $D = 150 \text{ nm}$ , (b)  $D = 500 \text{ nm}$ , and (c)  $D = 1000 \text{ nm}$ . The dark blue colored monopoles denote dislocations that have velocity magnitudes less than  $20 \text{ m/s}$  and that are essentially immobile.

torque,  $T/D^3$ , due to the inability to nucleate more dislocation loops, thus leading to a higher stress level. The dark blue colored monopoles denote dislocations that have velocity magnitudes less than  $20 \text{ m/s}$  and that are essentially immobile. Immobile dislocations in pile-ups occur at the center of the wire. The mobile dislocations can attain very high velocity magnitudes due to the linear mobility law, Eq. (16), and the high stresses that occur in the wires.

With  $D = 1000 \text{ nm}$ , Fig. 11c, more dislocation planes and sources are activated, leading to complex interactions between the mobile and immobile dislocations. These results are consistent with those of Senger et al. (2011) on wires having a  $\langle 100 \rangle$  orientation when cross-slip was not activated, showing no long dislocation segments along the torsion axis and that dislocation pile-ups occur perpendicular to it.

Further details about the dislocation configuration are given in Fig. 12 for the  $D = 1000 \text{ nm}$  wire of Fig. 11c using the same dislocation velocity scale. Here, dislocation monopoles on individual (active) slip systems are shown at  $\gamma_{\text{surf}}^p = 0.21 \%$ . The largest dislocation density occurs on the  $\{1\bar{1}1\}\langle 011 \rangle$ ,  $\bar{1}\bar{1}1\langle 1\bar{1}0 \rangle$ , and  $\bar{1}11\langle 110 \rangle$  slip planes. Due to the high dislocation activity near the surface of the wire, the fast-moving dislocations (red) lead to dislocations exiting the wire, inducing dislocation starvation. On other slip planes,

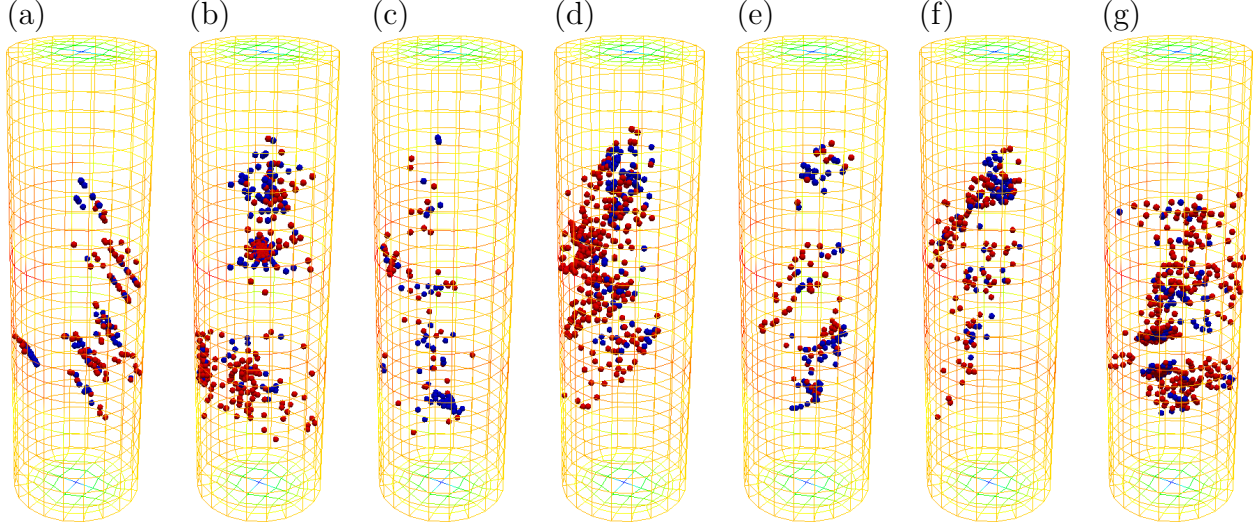


Figure 12: Monopole locations showing the dislocation configurations on active slip systems at  $\gamma_{\text{surf}}^p = 0.21\%$  with  $D = 1000\text{nm}$  and  $\rho_0 = 6 \times 10^{13} \text{m}^{-2}$ . (a)  $\{111\}\langle\bar{1}01\rangle$ , (b)  $\{1\bar{1}\bar{1}\}\langle 011\rangle$ , (c)  $\{1\bar{1}\bar{1}\}\langle\bar{1}01\rangle$ , (d)  $\{1\bar{1}\bar{1}\}\langle\bar{1}\bar{1}0\rangle$ , (e)  $\{1\bar{1}\bar{1}\}\langle 011\rangle$ , (f)  $\{1\bar{1}\bar{1}\}\langle 101\rangle$ , (g)  $\{1\bar{1}\bar{1}\}\langle 110\rangle$ . The dark colored monopoles denote dislocations that have velocity magnitudes less than 20 m/s and that are essentially immobile.

such as  $1\bar{1}1\langle\bar{1}01\rangle$ ,  $\bar{1}\bar{1}1\langle 011\rangle$ , and  $\bar{1}\bar{1}1\langle 101\rangle$ , there are trapped dislocations near the center of the wire, leading to dislocations being immobile there.

## 5 Concluding remarks

A three-dimensional, small strain discrete dislocation plasticity framework for solving quasi-static finite body boundary value problems has been presented that combines the monopole representation of dislocations with image fields that enforce the boundary conditions. In this framework, both the overall plastic flow and the evolving dislocation structure are outcomes of the boundary value problem solution. Torsional loading calculations were carried out for wires with diameters varying over three orders of magnitude and for two values of the initial dislocation density. The specimen size dependence and the dislocation structures that develop were investigated for single crystal wires subject to torsional loading. The calculations indicate that:

- There is a strong size-dependence of the torque, normalized by the cube of the wire diameter, with the scaling exponent of the size-dependence being dependent on specimen size with a less strong dependence on initial dislocation density.
- There is a transition with increasing wire diameter from nucleation controlled to interaction controlled dislocation plasticity with a strong size dependence in both these regimes. The interaction regime is dominated by the emergence of geometrically necessary dislocations and dislocation pile-ups perpendicular to the axis of twist. For wires

with a sufficiently large wire diameter, plastic deformation in the wire is much less heterogeneous and the dependence on size is greatly reduced.

- The capabilities of the discrete dislocation plasticity framework developed here can be enhanced by incorporating topological dislocation reactions leading to junction formation.
- The dislocation dynamics code used in the calculations was developed to explore the capabilities of the monopole representation. Computational efficiency can be much improved by parallelization of the code and by using a fast multipole method for the long range dislocation interaction calculations.

## Acknowledgments

AAB acknowledges support from NSF under grant CMMI-1950027. AC and AAB thank Vincent Chiaruttini and Jean-Didier Garaud from ONERA for assistance with the plugin interface of Z-set.

## Appendix A The elastic field of dislocation monopoles

For completeness, we collect the monopole velocity and stress fields, Eq. (5), resulting from classical and regularized linear elasticity.

### A.1 Green's function

The displacement field  $\mathbf{u}(\mathbf{x})$  of an infinite solid loaded by body forces  $\mathbf{f}(\mathbf{x})$  is a solution of Navier's equation

$$\frac{\partial}{\partial x_j} \left( c_{ijkl} \frac{\partial u_k}{\partial x_l}(\mathbf{x}) \right) + f_i(\mathbf{x}) = 0, \quad (\text{A-1})$$

where  $c_{ijkl} = c_{klij} = c_{jikl} = c_{ijlk}$  are the elastic moduli of the solid. The Green's function  $G_{ij}(\mathbf{x})$  is the  $i$ th component of the elastic field corresponding to a point load at the origin acting in the  $j$ th direction, i. e.,

$$\frac{\partial}{\partial x_j} \left( c_{ijkl} \frac{\partial G_{km}}{\partial x_l}(\mathbf{x}) \right) + \delta_{im} \delta(\mathbf{x}) = 0, \quad (\text{A-2})$$

where  $\delta(\mathbf{x})$  is Dirac's delta. For an isotropic elastic solid, the Green's function follows explicitly as

$$G_{ij}(\mathbf{x}) = \frac{1}{8\pi\mu} \left( \delta_{ij} \nabla^2 r - \frac{\lambda + \mu}{\lambda + 2\mu} \frac{\partial^2 r}{\partial x_i \partial x_j} \right), \quad (\text{A-3})$$

where  $r := |\mathbf{x}|$ ,  $\nabla^2$  is the Laplacian and  $\lambda$  and  $\mu$  are the Lamé constants.

## A.2 Displacement and stress fields

Consider a dislocation line in the form of a closed line  $C$ . The Burgers vector  $b_i(\mathbf{x})$  can change value at branching points of  $C$ , but it must be conserved according to Frank's rule. Then, Mura's formula (Mura (1963); cf. Hirth and Lothe (1982, eq. (4-12))) gives the displacement gradient as

$$\frac{\partial u_m}{\partial x_s}(\mathbf{x}) = \oint_C c_{ijkl} \frac{\partial G_{mk}}{\partial x'_l}(\mathbf{x}' - \mathbf{x}) e_{jsn} b_i(\mathbf{x}') dx'_n, \quad (\text{A-4})$$

whence the corresponding stress field follows from Hooke's law as

$$\sigma_{ij}(\mathbf{x}) = c_{ijkl} \frac{1}{2} \left( \frac{\partial u_k}{\partial x_l}(\mathbf{x}) + \frac{\partial u_l}{\partial x_k}(\mathbf{x}) \right), \quad (\text{A-5})$$

and the displacement field follows by Burgers' formula (cf. Hirth and Lothe (1982, eq. (4-6))) as

$$u_m(\mathbf{x}) = - \int_S c_{ijkl} \frac{\partial G_{mk}}{\partial x'_l}(\mathbf{x}' - \mathbf{x}) b_i(\mathbf{x}') dS_j(\mathbf{x}'), \quad (\text{A-6})$$

where  $dS_j(\mathbf{x})$  denotes the element of oriented area at  $\mathbf{x}$ . We note that the evaluation of Eq. (A-6) requires explicit knowledge of the slip surface  $S$  and cannot be reduced to a line integral. By contrast, the velocity field due to a moving dislocation line does reduce properly to a line integral. Thus, taking rates in Eq. (A-6) and applying Orowan's relation we obtain

$$\dot{u}_m(\mathbf{x}) = - \oint_C c_{ijkl} \frac{\partial G_{mk}}{\partial x'_l}(\mathbf{x}' - \mathbf{x}) e_{jpp} b_i(\mathbf{x}') v_p(\mathbf{x}') dx'_q(\mathbf{x}'), \quad (\text{A-7})$$

where  $v_p(\mathbf{x})$  denotes the velocity of the dislocation line  $C$  at  $\mathbf{x}$ .

## A.3 Monopole approximation

Approximating the dislocation distribution by a collection of monopoles and using the approximating property Eq. (1), the classical integral expressions of the stress and velocity fields, Eq. (A-4) and Eq. (A-7), become

$$\sigma_{pq}(\mathbf{x}) = \sum_{a=1}^M c_{pqms} c_{ijkl} \frac{\partial G_{mk}}{\partial x'_l}(\mathbf{x}_a - \mathbf{x}) e_{jsn} b_{ai} \xi_{an}, \quad (\text{A-8})$$

and

$$\dot{u}_m(\mathbf{x}) = - \sum_{a=1}^M c_{ijkl} \frac{\partial G_{mk}}{\partial x'_l}(\mathbf{x}_a - \mathbf{x}) e_{jpp} b_{ai} v_{ap} \xi_{aq}, \quad (\text{A-9})$$

respectively, where  $v_{ap} := (\mathbf{v}_a)_p$  is the velocity of monopole  $a$ . Thus, the discrete stress and velocity fields follow as the sum of monopole contributions, as surmised in Eq. (5) and expected from linearity.

## A.4 Core regularization

The stresses  $\boldsymbol{\sigma}(\mathbf{x})$  computed directly from linear elasticity as in Eq. (A-8) diverge as  $\mathbf{x}$  approaches one of the monopoles and Eq. (A-8) cannot be used directly to evaluate the self-forces of the monopoles in Eq. (13). One way to overcome this difficulty is to regularize linear elasticity and replace it by strain-gradient elasticity of the Mindlin type (Mindlin, 1964). A careful analysis (Deffo et al., 2019) shows that this regularization is equivalent to replacing the Green's function  $G$  of conventional linear elasticity in Eq. (A-8) and Eq. (A-9) by a regularized Green's function

$$G_{ij}^\epsilon(\mathbf{x}) = \iint G_{ij}(\mathbf{x} - \mathbf{x}' - \mathbf{x}'') \varphi^\epsilon(\mathbf{x}') \varphi^\epsilon(\mathbf{x}'') dV(\mathbf{x}') dV(\mathbf{x}''), \quad (\text{A-10})$$

where  $\epsilon$  is commensurate with the crystal lattice parameter and

$$\varphi^\epsilon(\mathbf{x}) = \frac{1}{4\pi\epsilon^2 r} e^{-r/\epsilon}, \quad r := |\mathbf{x}|, \quad (\text{A-11})$$

represents the core structure of the monopoles in Mindlin strain-gradient elasticity. For isotropic linear elasticity, Eq. (A-10) evaluates explicitly to (Deffo et al., 2019)

$$G_{ij}^\epsilon(\mathbf{x}) = \frac{1}{8\pi\mu} \left( \nabla^2 r^\epsilon \delta_{ij} - \frac{\lambda + \mu}{\lambda + 2\mu} \frac{\partial^2 r^\epsilon}{\partial x_i \partial x_j} \right), \quad (\text{A-12})$$

with

$$r^\epsilon := (r^2 + 4\epsilon^2 - \epsilon(r + 4\epsilon)e^{-r/\epsilon})/r. \quad (\text{A-13})$$

The regularized Green's function  $G_{ij}^\epsilon(\mathbf{x})$  is finite for  $\epsilon > 0$ . It can be readily verified that  $G_{ij}^\epsilon(\mathbf{x})$  converges to  $G_{ij}(\mathbf{x})$  in a distributional sense as  $\epsilon \rightarrow 0$ . In particular, the regularized stresses and velocities converge pointwise to the corresponding linear elastic fields in the same limit.

## References

- Ariza, M.P., Ortiz, M., 2021. A semi-discrete line-free method of monopoles for dislocation dynamics. *Extreme Mechanics Letters* 45, 101267.
- Arroyo, M., Ortiz, M., 2006. Local maximum-entropy approximation schemes: a seamless bridge between finite elements and meshfree methods. *International Journal for Numerical Methods in Engineering* 65, 2167–2202.
- Arsenlis, A., Cai, W., Tang, M., Rhee, M., Opperstrup, T., Hommes, G., Pierce, T.G., Bulatov, V.V., 2007. Enabling strain hardening simulations with dislocation dynamics. *Modell. Simul. Mater. Sci. Eng.* 15, 553–595.
- Ashby, M.F., 1970. The deformation of plastically non-homogeneous materials. *Philos. Mag.* 21, 399–424.

- Benzerga, A.A., 2008. An analysis of exhaustion hardening in micron-scale plasticity. *Int. J. Plast.* 24, 1128–1157.
- Bertin, N., Upadhyay, M.V., Pradalier, C., Capolungo, L., 2015. A FFT-based formulation for efficient mechanical fields computation in isotropic and anisotropic periodic discrete dislocation dynamics. *Modell. Simul. Mater. Sci. Eng.* 23, 065009.
- Bulatov, V.V., Abraham, F.F., Kubin, L., Devincere, B., Yip, S., 1998. Connecting atomistic and mesoscale simulations of crystal plasticity. *Nature* 391, 669–672.
- Bulatov, V.V., Cai, W., 2006. *Computer simulations of dislocations*. Oxford series on materials modelling. Oxford University Press, Oxford; New York.
- Cai, W., Arsenlis, A., Weinberger, C.R., Bulatov, V.V., 2006. A non-singular continuum theory of dislocations. *Journal of the Mechanics and Physics of Solids* 54, 561–587.
- Carrillo, J.A., Craig, K., Patacchini, F.S., 2019. A blob method for diffusion. *Calculus of Variations and Partial Differential Equations* 58, 53.
- Carrillo, J.A., Huang, Y., Patacchini, F.S., Wolansky, G., 2017. Numerical study of a particle method for gradient flows. *Kinetic and Related Models* 10, 613–641.
- Cleveringa, H.H.M., Van der Giessen, E., Needleman, A., 1999. A Discrete Dislocation Analysis of Bending. *Int. J. Plast.* 15, 837–868.
- Cleveringa, H.H.M., Van der Giessen, E., Needleman, A., 2000. A discrete dislocation analysis of mode I crack growth. *J. Mech. Phys. Solids* 48, 1133–1157.
- Comer, D., 1979. The ubiquitous B-tree. *Computing Surveys* 11, 121–137.
- Crone, J.C., Chung, P.W., Leiter, K.W., Knap, J., Aubry, S., Hommes, G., Arsenlis, A., 2014. A multiply parallel implementation of finite element-based discrete dislocation dynamics for arbitrary geometries. *Modelling and Simulation in Materials Science and Engineering* 22, 035014.
- Deffo, A., Ariza, M.P., Ortiz, M., 2019. A line-free method of monopoles for 3d dislocation dynamics. *Journal of the Mechanics and Physics of Solids* 122, 566 – 589.
- Deng, J., El-Azab, A., Larson, B., 2008. On the elastic boundary value problem of dislocations in bounded crystals. *Philosophical Magazine* 88, 3527–3548.
- El-Awady, J.A., 2015. Unravelling the physics of size-dependent dislocation-mediated plasticity. *Nature Communications* 6, 5926.
- Fedeli, L., Pandolfi, A., Ortiz, M., 2017. Geometrically exact time-integration mesh-free schemes for advection-diffusion problems derived from optimal transportation theory and their connection with particle methods. *International Journal for Numerical Methods in Engineering* 112, 1175–1193.

- Fleck, N.A., Muller, G.M., Ashby, M.F., Hutchinson, J.W., 1994. Strain gradient plasticity - theory and experiment. *Acta Metall. Mater.* 42, 475–487.
- Ghoniem, N.M., Tong, S.H., Sun, L.Z., 2000. Parametric dislocation dynamics: A thermodynamics-based approach to investigations of mesoscopic plastic deformation. *Phys. Rev. B* 61, 913–927.
- Gravell, J.D., Ryu, I., 2020. Latent hardening/softening behavior in tension and torsion combined loadings of single crystal fcc micropillars. *Acta Materialia* 190, 58–69.
- Greer, J.R., Oliver, W.C., Nix, W.D., 2005. Size dependence of mechanical properties of gold at the micron scale in the absence of strain gradients. *Acta Mater.* 53, 1821–1830.
- Hirth, J.P., Lothe, J., 1982. *Theory of Dislocations*. Wiley, New York.
- Hutchinson, J.W., 2000. Plasticity at the micron scale. *Int. J. Solids Struct.* 37, 225–238.
- Joa, J.A.G., Dupuy, L., Råback, P., Fivel, M., Perez, M., Amodeo, J., 2023. El-Numodis: a new tool to model dislocation and surface interactions. *Modell. Simul. Mater. Sci. Eng.* 31, 055003.
- Kysar, J.W., Gan, Y.X., Morse, T.L., Chen, X., Jones, M.E., 2007. High strain gradient plasticity associated with wedge indentation into face-centered cubic crystals: Geometrically necessary dislocation densities. *J. Mech. Phys. Solids* 55, 1554–1573.
- Lazar, M., 2017. Non-singular dislocation continuum theories: strain gradient elasticity vs. peierls–nabarro model. *Philosophical Magazine* 97, 3246–3275.
- Leiter, K.W., Crone, J.C., Knap, J., 2013. An algorithm for massively parallel dislocation dynamics simulations of small scale plasticity. *Journal of Computational Science* 4, 401 – 411.
- Liu, B., Huang, Y., Li, M., Hwang, K.C., Liu, C., 2005. A study of the void size effect based on the taylor dislocation model. *International Journal of Plasticity* 21, 2107–2122.
- Mindlin, R.D., 1964. Micro-structure in linear elasticity. *Arch. Rational Mech. Anal.* 16, 51–78.
- Mura, T., 1963. Continuous distribution of moving dislocations. *Phil. Mag.* 8, 843–859.
- Mura, T., 1982. *Micromechanics of Defects in Solids*. Martinus Nijhoff Publishers.
- Nicola, L., Xiang, Y., Vlassak, J.J., Van der Giessen, E., Needleman, A., 2006. Plastic deformation of freestanding thin films: Experiments and modeling. *J. Mech. Phys. Solids* 54, 2089–2110.
- Nix, W.D., Gao, H., 1998. Indentation size effects in crystalline materials: A law for strain gradient plasticity. *J. Mech. Phys. Solids* 46, 411–425.



- Nye, J.F., 1953. Some geometrical relations in dislocated crystals. *Acta Metallurgica* 1, 153–162.
- Pandolfi, A., Stainier, L., Ortiz, M., 2023. An optimal-transport finite-particle method for mass diffusion. *Computer Methods in Applied Mechanics and Engineering* 416, 116385.
- Ryu, I., Gravell, J., Cai, W., Nix, W.D., Gao, H., 2020. Intrinsic size dependent plasticity in bcc micro-pillars under uniaxial tension and pure torsion. *Extreme Mechanics Letters* 40, 100901.
- Senger, J., Weygand, D., Kraft, O., Gumbsch, P., 2011. Dislocation microstructure evolution in cyclically twisted microsamples: a discrete dislocation dynamics simulation. *Modell. Simul. Mater. Sci. Eng.* 19, 074004.
- Stölken, J.S., Evans, A.G., 1998. A microbend test method for measuring the plasticity length scale. *Acta Mater.* 46, 5109–5115.
- Uchic, M.D., Shade, P.A., Dimiduk, D.M., 2009. Plasticity of micrometer-scale single crystals in compression. *Annu. Rev. Mater. Res* 39, 361–386.
- Van der Giessen, E., Needleman, A., 1995. Discrete dislocation plasticity: a simple planar model. *Modell. Simul. Mater. Sci. Eng.* 3, 689–735.
- Vattré, A., Devincere, B., Feyel, F., Gatti, R., Groh, S., Jamond, O., Roos, A., 2014. Modelling crystal plasticity by 3D dislocation dynamics and the finite element method: The Discrete-Continuous Model revisited. *J. Mech. Phys. Solids* 63, 491–505.
- Weinberger, C.R., Aubry, S., Lee, S.W., Nix, W.D., Cai, W., 2009. Modelling dislocations in a free-standing thin film. *Modelling and Simulation in Materials Science and Engineering* 17, 075007.
- Weygand, D., Friedman, L.H., Van der Giessen, E., Needleman, A., 2002. Aspects of boundary-value problem solutions with three-dimensional dislocation dynamics. *Modell. Simul. Mater. Sci. Eng.* 10, 437–468.
- Z-set, 2020. Non-linear material & structure analysis suite Z-set 9.1. Mines ParisTech and French Aerospace Lab (ONERA), Paris, France.
- Zbib, H., Rhee, M., Hirth, J.P., 1998. On plastic deformation and the dynamics of 3D dislocations. *Int. J. Mech. Sci.* 40, 113–127.